NJC

ROYAL SOCIETY OF CHEMISTRY

PAPER

View Article Online
View Journal | View Issue

Cite this: *New J. Chem.*, 2021, 45, 13833

Synergistic effect of Fe and Ga incorporation into ZSM-5 to increase propylene production in the cracking of *n*-hexane utilizing a microchannel reactor

Mohsen Rostami Sakha,[ab] Saeed Soltanali,*[b] Darush Salari,[a] Mehdi Rashidzadeh[b] and Parya Halimitabrizi[ac]

In the present study, the effect of various amounts of Fe and Ga in the catalytic cracking of *n*-hexane in a microchannel reactor was investigated using experimental design by the D-optimal method. Nano zeolites incorporated with Fe and Ga metals were synthesized in a fluorine environment to investigate the synergistic effect of the metals on the textural and acidic properties of the catalysts, which ultimately improved the performance of the synthesized catalysts in the efficient production of light olefins, in particular propylene. Three synthesis parameters including the Si/Al, Si/Fe and Si/Ga ratios were considered as the main factors to determine the optimal conditions for obtaining the maximum conversion of *n*-hexane, yield of light olefins, and P/E ratio and minimum yield of alkanes as the responses. In sample FeGa-1, the P/E ratio reached 3.97, indicating the significant effect of the substituted metals in improving the desirable routes for propylene production. According to the results of the acidic properties, Fe, Al and Ga increased the number of total acid sites and the strengths of strong and weak acid sites, respectively. In addition, according to the results obtained from sample FeGa-7, the synergistic effect of Fe and Ga increased the number of weak acid sites.

Received 16th April 2021,
Accepted 27th June 2021

DOI: 10.1039/d1nj01866c

rsc.li/njc

1. Introduction

As expected, light olefins with a trade of about $1 trillion by 2025 are one of the main chemical products. Meanwhile, the global demand for propylene surpasses that of ethylene as the U.S.A's second largest produced chemical, doubling the importance of increasing the production efficiency of this raw material widely used in the production of chemicals, including polypropylene, acrylonitrile, propylene epoxide and acetone.[1–5] Conventional methods for light olefin production include methanol to olefin conversion (MTO), steam cracking of naphtha (SCN) and fluid catalytic cracking (FCC).[6–9] As propylene is a byproduct of olefin production processes, the need for technologies which increase the production efficiency of propylene is felt. In other words, on-purpose production of propylene should be achieved through using novel reactors and catalysts.[10,11] The SCN process cannot meet the needs of the global market for propylene as the main propylene production process due to emission of greenhouse gases such as CO_2, high energy consumption at high temperatures (>800 °C) and the low propylene/ethylene ratio.[12] One of the approaches to overcome the limitations of this process is the utilization of stable and efficient catalysts.

Shape selective catalysts as solid acids are suitable choices for this process because they increase the selectivity to the desired products by sieving the reactants, intermediates and products based on their pore structure and size.[13–16] The ZSM-5 zeolite, which consists of tetrahedral units causing negative charges in the lattice by bonding Si atoms to Al atoms *via* oxygen bridges, is the most commonly used MFI topology in isomerization, cracking, aromatization and alkylation processes.[17–19] By neutralizing the negative charges by cations (K^+, Na^+, Cs^+, Li^+ and H^+), Brønsted acid sites (BAS) will form.[20,21] ZSM-5 has 12 orthorhombic distinct T-sites in which sites T4, T10 and T8, T11 are accessible on the sinusoidal and straight channels, respectively.[14,22]

The framework Al position and distribution in high-Si zeolites are not random or controlled by statistical rules.[23,24] Since most of the acid sites are Al-dependent, their positioning at different T-sites affects the catalytic performance of the zeolites.[25] Al forms Lewis acid sites (LAS) by being located outside the zeolite structure (extra-framework Al).[13,26,27]

[a] *Reactor and Catalysis Research Lab., Department of Chemistry, University of Tabriz, Tabriz, Iran*
[b] *Catalysis Technologies Development Division, Research Institute of Petroleum Industry (RIPI), Tehran, Iran. E-mail: sssoltan@gmail.com, soltanalis@ripi.ir*
[c] *Department of Chemical and Petroleum Engineering, University of Tabriz, Tabriz, Iran*

Framework Al changes the accessibility of steric molecules as well as the acidic strength by incorporating in different T-sites.[28] BAS (tetrahedral framework Al) alter the enthalpic and entropic effects and selectivity of products through incorporation in straight and sinusoidal channels or intersections.[21] Investigations have proved that the incorporation of BAS in the channels encourages an alkene-based cycle and propylene selectivity in the MTO process. In addition, the propylene selectivity was also increased in the cracking of alkanes and alkenes by incorporation of Al in the channels.[19,29–33] The combination of using TPAOH, colloidal silica,[30,31,34] NH_4F[11,35,36] and Na^+ as the organic structure directing agent (OSDA), Si source, mineralizer and inorganic compensating cation, respectively, results in more incorporation of Al and possibly other metals in the channels.[10,17,30,37]

Conventional zeolites are predominantly microporous, limiting the transport of reactants, intermediates and products. Various methods including the preparation of nano-sized, mesoporous and hollow zeolites have been developed to overcome the limitations of mass transfer.[38] Mesoporous structures increase the activity and selectivity to the desired products by facilitating access to acid sites and rapid exit of the main products produced, and avoiding side reactions and formation of aromatics as precursors of coke deposition. On the other hand, the size of the cavities formed in hierarchical structures should not be too large because larger cavities will form larger molecules such as BTX and decrease the propylene selectivity.[2,3,8,31,39–44] Hard-templating, post-treatment and soft-templating are common methods to form hierarchical structures. Various groups have recently reported novel methods for the synthesis of hierarchical ZSM-5 by optimization of the gelation and crystallization conditions as well as synthesis in fluoride medium as the nucleation and/or mineralization agent.[31,34,45]

One of the main approaches to increase the yield of light olefins and the lifetime of zeolites is the modification of the acidity using various elements. Conventional methods for metal modification are impregnation (wet or dry) and ion exchange. Another method to modify the structural and acidic properties of zeolites is incorporation. Meanwhile, the ion exchange and impregnation methods often cause the formation of extra-crystalline metal oxides.[46] The incorporation of Fe and Ga improves the selectivity of light olefins and the stability of ZSM-5 by reducing the acidic strength. On the other hand, the higher distribution of extra-framework Ga species, which exist in various forms of Ga^+, GaO^+, $Ga_2O_2^{2+}$, GaH_2^+, GaH^{2+}, $Ga(OH)_2^+$ and $GaH(OH)^+$, improves the selectivity of arenes by enhancing dehydrogenation reactions near protonic sites.[47–57]

Experimental design methods have been used in catalytic fields for many years, including the design of catalytic reactors, the formulation and preparation of catalysts, and the kinetic modeling of catalysts. The purpose of experimental design can be achieved by repeating the experiments several times so that each of the parameters which affect the synthesis can be examined alone along with constant consideration of the other parameters. This means that without the use of experimental design, the required time and labor during the process of achieving the optimal catalyst composition is significantly increased. This in turn leads to an increase in the use of raw materials, and, due to the possibility of consumables being toxic in the production of catalysts, increasing the amount of consumption of these materials can lead to irreparable damage to the environment. Experimental design methods define an experimental area (the range of parameter values) in which a mathematical model is defined to estimate the effect of the survey parameters. The D-optimal experimental design method, as the most up-to-date method, is used in cases where the test areas are irregular, pre-designed tests should be added to the design tables, the quantitative factors have more than 2 levels, the number of tests should be reduced and special regression models should be adapted, and process and mixing factors must be used simultaneously in a design.[58–60]

In this investigation, the synergistic effect of Fe and Ga incorporation into the zeolite structure in the catalytic cracking of *n*-hexane as well as the acidic and structural properties have been investigated for the first time. Microchannels were used as novel reactors to increase the activity and stability of the obtained catalysts by enhancing mass and heat transfer. XRD, FE-SEM, EDX elemental mapping, BET, NH_3-TPD and H_2-TPR analyses were applied to determine the intrinsic properties of the synthesized catalysts. The D-optimal method was also used in the experimental design of 12 experiments to demonstrate the effect of the Si/Al, Si/Fe and Si/Ga factors on the four responses. The valid interactions of the variable factors in the conversion, yield of light olefins, P/E ratio and yield of alkanes were determined as the responses. Moreover, the optimum conditions for maximum production of propylene *via n*-hexane cracking were estimated.

Table 1 Investigated parameters and their levels

Factor	Name	Type	Low level (−1)	High level (+1)
A	Si/Al	Numerical	100	400
B	Si/Fe	Numerical	100	400
C	Si/Ga	Numerical	100	400

Table 2 The responses and experimental design for three independent variables

	Factors				Responses		
Run	*A*	*B*	*C*	Conversion (%)	Alkane yield (%)	$(C_2^= + C_3^=)$ yield (%)	P/E
1	400	220	279	71.4	18.9	37.3	3.97
2	400	400	100	89.6	22.4	51.2	2.83
3	221	400	279	93.6	27.2	51.1	2.52
4	213	213	287	85.3	25.1	44.7	2.97
5	310	317	175	87.3	20.5	50.1	3.62
6	291	100	400	73.6	19.1	39.4	3.48
7	400	100	100	79.8	18.1	44.4	3.52
8	222	222	100	96.0	25.8	52.0	2.13
9	100	100	203	84.4	22.9	45.4	3.48
10	100	400	100	97.3	27.9	52.9	1.92
11	100	100	395	84.4	23.3	45.1	2.74
12	100	294	400	95.3	30.4	49.0	1.95
13	400	400	400	79.2	23.5	40.0	3.20

2. Experimental

2.1. Catalyst preparation

Zeolites were hydrothermally synthesized in fluoride medium. Aluminum sulphate ($Al_2(SO_4)_3{\cdot}18H_2O$, Merck Chemical Co.) and colloidal silica (40 wt% SiO_2, Aldrich Chemical Co.) were used as Al and Si sources, respectively, to increase the incorporation of Al in the framework. The main molar composition of the solutions was $SiO_2{:}xAl_2O_3{:}yFe_2O_3{:}zGa_2O_3{:}0.2TPAOH{:}0.19Na_2O{:}0.205NH_4F{:}32H_2O$ (x, y and z were calculated from Tables 1 and 2). Firstly, a solution containing NH_4F, aluminum(III) sulfate, iron(III) nitrate and $GaCl_3$ (their amounts were carefully calculated according to the different ratios in Table 2 and added to the solution following NH_4F at the same time) was prepared and then the solution was stirred at ambient temperature for 20 minutes. After obtaining a clear solution, colloidal silica, NaOH, and TPAOH were added to form a white gel. The gel was then aged at room temperature for 24 h at 300 rpm. The zeolites were crystallized dynamically at 180 °C for 72 h at 300 rpm followed by centrifuging, drying and calcination at 550 °C for 6 h. H-ZSM-5 was obtained by ion-exchanging the powder with NH_4NO_3 (1 M) at 80 °C two times, followed by calcination at 550 °C for 6 h.

2.2. Characterization

XRD (X-ray diffraction) patterns were acquired on an Inel EQUINOX 3000 X-ray diffractometer with Cu Kα radiation at 40 kV and 100 mA. All spectra were collected in the 2θ = 7–50° range with a step size of 0.02°.

Scanning electron microscopy (SEM) and energy dispersive X-ray analysis (EDX) were performed to determine the presence of various elements and the morphology of the zeolites. SEM and EDX maps were obtained using a Zeiss Sigma VP field emission scanning electron microscope (FE-SEM).

The textural properties of the synthesized catalysts were characterized using a Micromeritics instrument from the BET model by N_2 adsorption–desorption at 77 K. The samples were first outgassed under a vacuum (<0.5 Pa) for 7 h before N_2 physisorption. The external surface areas were determined by the Brunauer–Emmett–Teller (BET) method using the desorption data in the relative pressure (p/p^0) range of 0.01–0.99. The pore size distribution and the contribution from both micro- and mesoporosity were derived using the t-plot and the Barrett–Joyner–Halenda (BJH) model.

NH_3 temperature-programmed desorption (NH_3-TPD) and H_2 temperature-programmed reduction (H_2-TPR) were carried out using a Micromeritics TPR/TPD 2900 chemisorption analyzer. NH_3-TPD and H_2-TPR were used to determine the number and strength of acid sites and evaluate the reducibility of the synthesized catalysts, respectively. For NH_3-TPD evaluation about 0.2 g of zeolite was pre-treated under a flow of He at 550 °C for 1 h and then cooled down to 150 °C. Afterwards, ammonium was introduced into the flow system. Finally, the TPD curves were acquired using the NH_3 saturated sample in the temperature range of 150–600 °C at a ramping speed of 10 °C min^{-1}. As for the H_2-TPR investigation, 0.2 g of zeolite was pre-treated at 500 °C under an N_2 flow (30 mL min^{-1}) and then cooled down to 100 °C. Afterwards, the N_2 flow was changed to a mixture of H_2/N_2. The TPR profiles were then obtained by reducing the samples under the mixture of H_2 and N_2 pulses (H_2/N_2 = 10%) with temperature raised to 700 °C at a ramping rate of 10 °C min^{-1}.

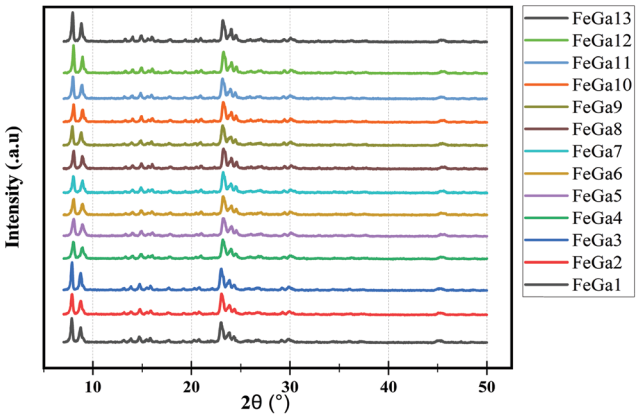

Fig. 1 XRD patterns of HZSM-5 catalysts synthesized using various amounts of Al, Fe and Ga.

2.3. Catalytic performance

Catalytic tests for the catalytic cracking of n-hexane were performed in a reactor with 5 microchannels with dimensions of 50 × 1 × 1 mm at T = 600 °C and atmospheric pressure under an N_2 flow as the carrier gas. Each time the test was performed, 0.125 g of meshed zeolite (sieve fraction 150–250 μm) was packed in the microchannels. The catalyst was activated *in situ* by heating at 550 °C for 2 h in a 30 cc per min N_2 flow. The outlet gas was analyzed after an hour's reaction. The products were analyzed using an online gas chromatograph (Shimadzu 2010 Plus GC) equipped with a flame ionization detector (FID) with an HP-PLOT Al_2O_3 capillary column, every hour during the 6 h of reaction.

2.4. D-Optimal experimental design

In order to improve the properties of ZSM-5 and optimize the amount of substituted metals in the structure of the synthesized catalysts, experimental design was used with three numerical factors due to advantages such as reduced costs, a decreased number of tests, a comprehensive review of the system under study and the capability to optimize the desired values of the answers with the input variables. In this research, the D-optimal design method was applied to optimize the quantitative value of the Si ratio to each of the substituted metals (Al, Fe and Ga) and estimate the performance of the prepared catalysts in the catalytic cracking of n-hexane. The main and interaction effects along with the analysis of variance (ANOVA) on the conversion, yield of alkanes, yield of propylene and ethylene and P/E ratio were evaluated as quantitative responses. As shown in Tables 1 and 2, Design-Expert software (Version 7.0.0) was used to evaluate the responses of the Si/Al (A), Si/Fe (B) and Si/Ga (C) factors with a sum of 12 experiments. The D-optimal design of experiment and experimental results are displayed in

Fig. 2 FE-SEM images of the zeolites.

Table 3 Particle size of the synthesized zeolites obtained from SEM images

Catalyst sample	Particle size (μm)
FeGa-1	6.5
FeGa-2	7.7
FeGa-3	9.2
FeGa-4	7.7
FeGa-5	1.3
FeGa-6	4.2
FeGa-7	4.9
FeGa-8	6.6
FeGa-9	8.8
FeGa-10	11.5
FeGa-11	9.5
FeGa-12	9.1
FeGa-13	3.2

Tables 1 and 2. The experimental results were obtained by carrying out the experiments randomly to avoid any systematic bias.

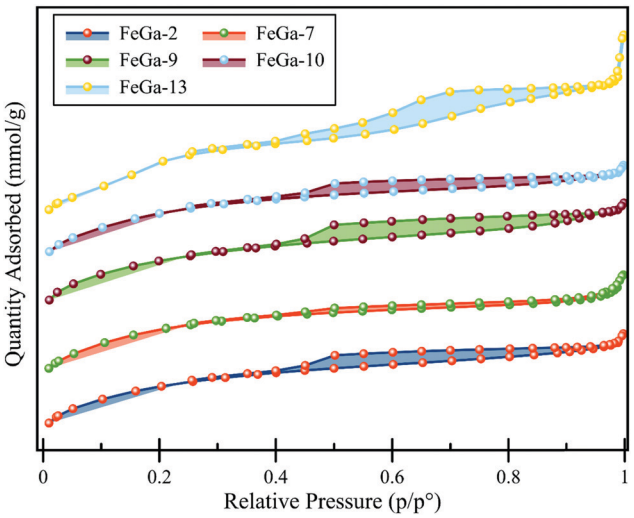

Fig. 4 N_2 adsorption–desorption isotherms of the samples.

3. Results and discussion

3.1. Textural properties

In the X-ray patterns (Fig. 1), the peaks corresponding to Fe and Ga oxides are not visible, which can result from the incorporation of metals into the zeolite framework or at least the excellent distribution of metals in the cavities and surface. In addition, the typical peaks of the MFI topology structure were observed, confirming the successful synthesis of pure zeolites.[61]

According to the SEM images (Fig. 2), all the synthesized zeolites with various Si/M ratios showed the same uniform spherical morphology resulting from the aggregation of nanospheres. The comparison of the particle sizes in Table 3 showed that reducing the Si/Al ratio simultaneously with decreasing the Si/Ga ratio caused a significant increment in the particle size (FeGa-10). In contrast, reducing the Si/Ga ratio individually led to a much smaller increase in the particle size (FeGa-2). On the other hand, the simultaneous decrease of the Si/Ga and Si/Fe ratios did not have a considerable effect on the particle size, which probably indicates the synergistic nature of Fe and Ga metals in the reduction of the particle size (FeGa-7). It seems that increasing the amount of Ga along with a slight growth in the amounts of Fe and Al in the zeolite structure reduces the particle size by strengthening the nucleation and growth rate of the crystals (FeGa-5).[47] The atomic radii of Fe, Al, and Ga are 126, 143, and 135 pm, respectively. Considering the various atomic radii of the metals, the particle size increased with the increment of Al and Ga, but increasing Fe reduced the average atomic radii of the formed particles and the particle size decreased dramatically. In addition, careful observation of the SEM images shows that no cloud-like layers were formed, which generally indicates the presence of impurities and/or the formation of metal oxides on the surface of the particles. As observed in Fig. 3, the obtained maps of FeGa-13 synthesized using equal amounts of metals demonstrated the symmetric distribution of all metals in different parts of the particles. According to the IUPAC classification, all synthesized zeolites demonstrated a combination of type I and IV isotherms (Fig. 4) accompanied by capillary condensation due to the sharp uptake at very low pressure and hysteresis loop at higher pressure ($p/p^0 > 0.4$).[45,47,62] The combination feature of the isotherms indicates the coexistence of narrow micropores (<1 nm) and mesopores (<2.5 nm) as well as wider mesopores (>4 nm), which is mainly due to the formation of homo-

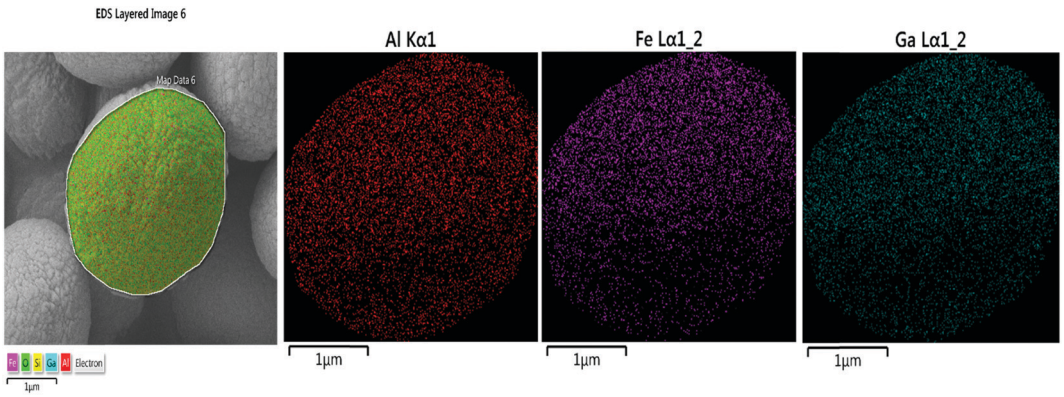

Fig. 3 EDX maps of FeGa-13 for the Al, Fe and Ga elements.

Table 4 Textural properties of the zeolite samples

Catalyst	S_{BET}[a]	S_{ext}[b]	S_{ext}/S_{BET}	V_t[c]	V_{mic}[d]	V_{mes}[e]	d[f]
FeGa-2	392	282	0.71	0.180	0.059	0.121	1.88
FeGa-7	391	280	0.71	0.180	0.059	0.121	1.90
FeGa-9	413	296	0.71	0.197	0.066	0.131	1.90
FeGa-10	400	289	0.72	0.180	0.062	0.118	1.86
FeGa-13	378	255	0.67	0.213	0.056	0.157	2.25

[a] The specific surface area ($m^2\ g^{-1}$). [b] The external surface area ($m^2\ g^{-1}$). [c] The total pore volume ($cm^3\ g^{-1}$). [d] The micropore volume ($cm^3\ g^{-1}$). [e] The mesopore volume ($cm^3\ g^{-1}$). [f] The average pore diameter (nm).

geneous nanocrystals. Moreover, according to Table 4, the distribution of the micropore and mesopore volumes of the samples confirms the pore size distribution and also the simultaneous formation of type I and IV isotherms. This is in agreement with the SEM results. Moreover, all synthesized zeolites using different amounts of metals displayed a sharp desorption peak in the range of $p/p^0 > 0/4$, which is one of the main features of H_2 type hysteresis loops. The combination of H_2 and H_4 type hysteresis loops (due to more pronounced uptake at low p/p^0) indicates the formation of smaller mesopores and more interconnections between the crystals. In addition, the combination of hysteresis loops represents neck obstruction of the micropores and mesopores, most likely due to the formation of non-framework species with the presence of Fe and Ga, which have different inherent properties from Al. In addition, the H_4 type hysteresis loop confirms the accumulation of ultra-uniform nanocrystals, which is verified by the SEM results. Smaller mesopores were also evident in the pore size distribution profiles because the samples had a smaller number and smaller pore size distribution, with the exception of sample FeGa-13. In FeGa-13, Fe, Ga, and Al were probably more evenly distributed than the other samples due to the equal amount of metals.

3.2. Acidic properties

Fig. 5 and Table 5 display the results obtained from NH_3-TPD analysis of the synthetic zeolites with different incorporated

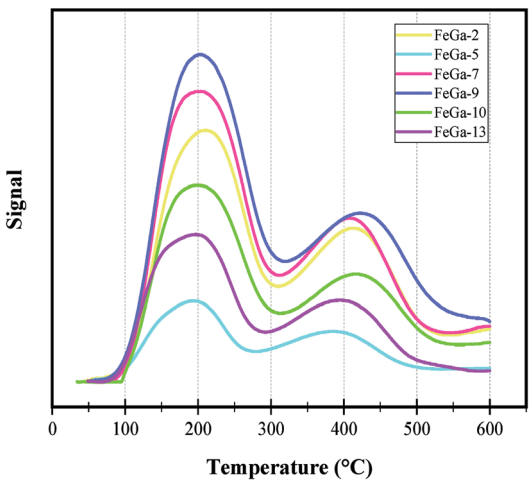

Fig. 5 NH_3-TPD plot of HZSM-5 catalysts synthesized using various amounts of Al, Fe, and Ga.

Table 5 Concentration of weak and strong acid sites according to NH_3-TPD

Catalyst	Total acid (mmol g^{-1})	Weak acid (mmol g^{-1})	Strong acid (mmol g^{-1})	T_W[a] (°C)	T_S[b] (°C)	W/S
FeGa-2	0.140	0.090	0.050	210	414	1.80
FeGa-5	0.043	0.027	0.016	194	386	1.68
FeGa-7	0.178	0.117	0.061	202	409	1.91
FeGa-9	0.187	0.127	0.060	203	424	2.11
FeGa-10	0.122	0.087	0.040	201	417	2.05
FeGa-13	0.082	0.053	0.029	197	393	1.83

[a] The temperature related to the weak acidity zone. [b] The temperature related to the strong acidity zone.

amounts of Fe, Ga and Al. According to Tables 2 and 5, with increasing the total amounts of substituted metals, the total acidity increased remarkably (except for sample FeGa-5). Samples FeGa-13, FeGa-7 and FeGa-10 clearly illustrated an increase in the number of total acid sites with increasing the amount of metals. FeGa-7 and FeGa-10 had a constant Si/Ga ratio, but as the amount of the other metals changed, the total acid sites increased. The comparison of the total acid sites of the two samples (0.178 *vs.* 0.122 mmol g^{-1}) demonstrated that, as the amount of Fe increased, the total acidity increased to a much greater extent than with the increment of Al. The comparison of the corresponding temperature to the weak acid site (WAS) zone (150–250 °C) also showed that, with increasing the amount of metals, the strength of WAS increased due to the desorption of ammonium at higher temperature. The comparison of samples FeGa-7 and FeGa-10 with equal Si/Ga ratios showed that the Fe and Al metals alone do not play a role in enhancing the strength of WAS since the alteration in the amount of Fe and Al did not cause a significant difference in the ammonium desorption temperature corresponding to the WAS. However, according to FeGa-2, increasing the amount of Ga increased the strength of the WAS. Therefore, the amount of Ga is an influential factor to enhance the strength of WAS, which is likely to improve olefin production processes. The comparison of the ammonium desorption temperature corresponding to the strong acid site (SAS) zone (375–500 °C) showed that the strength of SAS, which are predominantly related to the strong Brønsted acid sites (SBAS),[30,53] increased with increasing the amount of metals due to the temperature shift toward higher temperatures. As observed in the NH_3-TPD plot of samples FeGa-7 and FeGa-10, the temperatures corresponding to the SAS zone were equal to 409 and 417 °C, respectively, which indicates increasing the strength of SAS in the sample with an increased amount of Al (FeGa-10). The comparison of the number of WAS and SAS of the synthesized zeolites using different ratios of Fe, Ga and Al showed attractive consequences from the synergistic effect of Fe and Ga atoms. According to Tables 2 and 5, increasing Ga alone led to a significant increase in the number of WAS in sample FeGa-2. On the other hand, increasing the amount of Al simultaneously with Ga in equal amounts reduced the number of weak, strong and total acid sites in the FeGa-10 sample. It was expected that in this sample, due to the higher amount of metals incorporated into the zeolite, the formation of more acid sites would be observed, but, contrary to expectations, not only did the amount of total acid

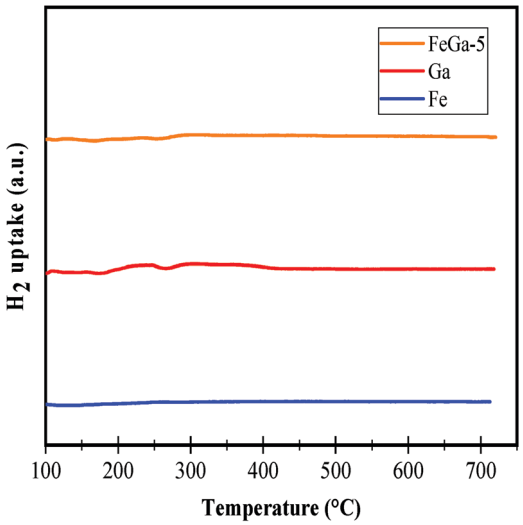

Fig. 6 H_2-TPR profiles of FeGa-5, FeZSM-5 and GaZSM-5.

sites decrease compared to sample FeGa-2, but the numbers of SAS and WAS were also reduced. This phenomenon indicates the undeniable effect of the Ga metal on the increasing active sites, especially WAS, in the synthesis of ZSM-5 zeolites. In sample FeGa-7, decreasing the amount of Al and increasing the amount of Fe in equal proportions increased the number of total acid sites as well as significantly increasing the number of WAS as the main active centers to direct the reaction path toward the production of light olefins, especially propylene.

Temperature programmed reduction *via* hydrogen analysis was used to determine the distribution of Ga and Fe atoms. The comparison of the H_2-TPR curves of sample FeGa-5 and zeolites incorporated with Fe and Ga metals alone is shown in Fig. 6. According to the diagram, no peaks corresponding to Fe and Ga species were observed. The reduction of extra-framework GaO^+ to Ga^+ at temperatures above 710 °C has clear peaks. In addition, the reduction of Ga_2O_3 at a lower temperature in the range of 500–570 °C possesses an obvious peak. The reduction of iron oxides also shows peaks in the temperature ranges of 300–400 °C and 400–700 °C. The absence of peaks in these areas indicated the major incorporation of metals into the structure of the synthesized zeolites and/or a lack of reducible extra-framework gallium species. This phenomenon has occurred due to the presence of NH_4F as a mineralizer agent as well as low amounts of Fe and Ga metals. The use of this compound results in the formation of $(NH_4)_3GaF_6$ solution, the hydrolysis of which forms $Ga(OH)_3$. The complete incorporation of gallium hydroxide in the hydroxyl cavities and/or tetrahedral structure of the zeolites has reduced or eliminated gallium oxides or extra-structural species. Reducible extra-framework gallium species, the absence of which is one of the intrinsic reasons for the low selectivity of aromatics, are the active acid sites for the production of aromatics *via* dehydrogenation processes. Therefore, it can be claimed that the maximum modifications have been made to reduce the production of aromatics. It should be noted that the results of this analysis confirm those of the XRD and SEM analyses.[47]

3.3. Analysis of variance

According to Table 6, a total of 12 experiments were performed using the D-optimal method. Significant and insignificant parameters can be determined using the Fischer variance ratios of the parameter effect dispersion to the error dispersion. The *F*-test is used to compare the statistical models with the experimental data. The higher the fit between the model and the data, the higher the exact value of *F*. In this research, a 95% confidence interval has been used to evaluate the significance of the parameters. Therefore, a probability value (*p*-value) of 0.05% would be a significant level in the *F*-tests for the interpretation of the effects. In the present study, analysis of variance was used to quantitatively investigate the effects of the input variables on the responses. The results are presented in the ANOVA table (Table 6).

The suitable R_2 and high *F*-value of the model imply the ability of the models for prediction of responses. *F* shows the probability of model error; therefore, a small value of *F* indicates that the model is correct. The polynomial predictive models for the responses developed by the model are presented in Table 7, based on the coded value.

Table 6 ANOVA result for the model

	Conversion (*R1*)		Yield (C_1–C_4) (*R2*)		Yield (C_2^-–C_3^-) (*R3*)		P/E (*R4*)	
Source	*F* value	*p*-value	*F* value	*p*-value	*F* value	*p*-value	*F* value	*p*-value
Model	82.15	<0.0001	23.59	0.0002	47.52	<0.0001	13.44	0.0011
A	316.31	<0.0001	33.52	0.0002	102.10	<0.0001	23.45	0.0009
B	205.33	<0.0001	20.76	0.0010	81.72	0.0001	12.63	0.0062
C	87.62	0.0002	—	—	90.33	<0.0001	—	—
AB	—	—	—	—	—	—	—	—
AC	40.86	0.0014	—	—	31.60	0.0014	—	—
BC	20.17	0.0065	—	—	—	—	—	—
A^2	36.79	0.0018	—	—	21.48	0.0036	—	—
B^2	—	—	—	—	—	—	—	—
C^2	27.63	0.0033	—	—	6.71	0.0412	9.14	0.0144
Model statistics								
R^2	0.9914		0.8251		0.9794		0.8175	
R^2 adj.	0.9793		0.7901		0.9588		0.7567	
R^2 pred.	0.9103		0.7238		0.8855		0.6587	

Table 7 Final models in terms of actual factors for responses

Responses		Final model
Conversion ($R1$)	R-square 0.9914 Adjusted R-square 0.9793 Predicted R-square 0.9103	$R1 = +86.04 - 7.94 \times A + 6.38 \times B - 3.99 \times C - 3.34 \times A \times C + 2.35 \times B \times C - 4.83 \times A^2 + 4.35 \times C^2$
Yield (C_1–C_4) ($R2$)	R-square 0.8271 Adjusted R-square 0.7901 Predicted R-square 0.7238	$R2 = +23.47 - 3.49 \times A + 2.74 \times B$
Yield ($C_2^=$–$C_3^=$) ($R3$)	R-square 0.9794 Adjusted R-square 0.9588 Predicted R-square 0.8855	$R3 = +46.87 - 3.77 \times A + 3.50 \times B - 3.53 \times C - 2.55 \times A \times C - 3.18 \times A^2 + 1.84 \times C^2$
P/E ($R4$)	R-square 0.8175 Adjusted R-square 0.7567 Predicted R-square 0.6581	$R4 = +3.36 + 0.56 \times A - 0.41 \times B - 0.63 \times C^2$

3.3.1. Regression model. To implement the D-optimal method, a mathematical model must first be selected to correlate the independent variables with the dependent ones. In this research, the most common method, namely the quadratic model of the equation, was used. In D-optimal design, it is possible to modify the quadratic model in any way. Thus, in the case of insignificant effects, some parameters can be removed without negatively affecting the results.

The general form of the quadratic model is presented as eqn (1). In this equation, Y is the studied response, X_i and X_j are the variables considered in the study and β_0, β_i and β_{ji} are the estimated coefficients. A combination of factors (such as X_iX_j) represents the interactions between the individual factors in that term.

$$Y = \beta_0 + \sum_{i=1}^{k} \beta_i X_i + \sum_{i=2}^{k} \beta_{ii} X_i^2 + \sum_{i<j}^{\sum} \beta_{ij} X_i X_j + \varepsilon \qquad (1)$$

The experimental results and the predicted coefficients of the equation for the system responses are shown in Fig. 7. As observed, the predicted coefficients are in good agreement with the experimental values obtained from the experiments

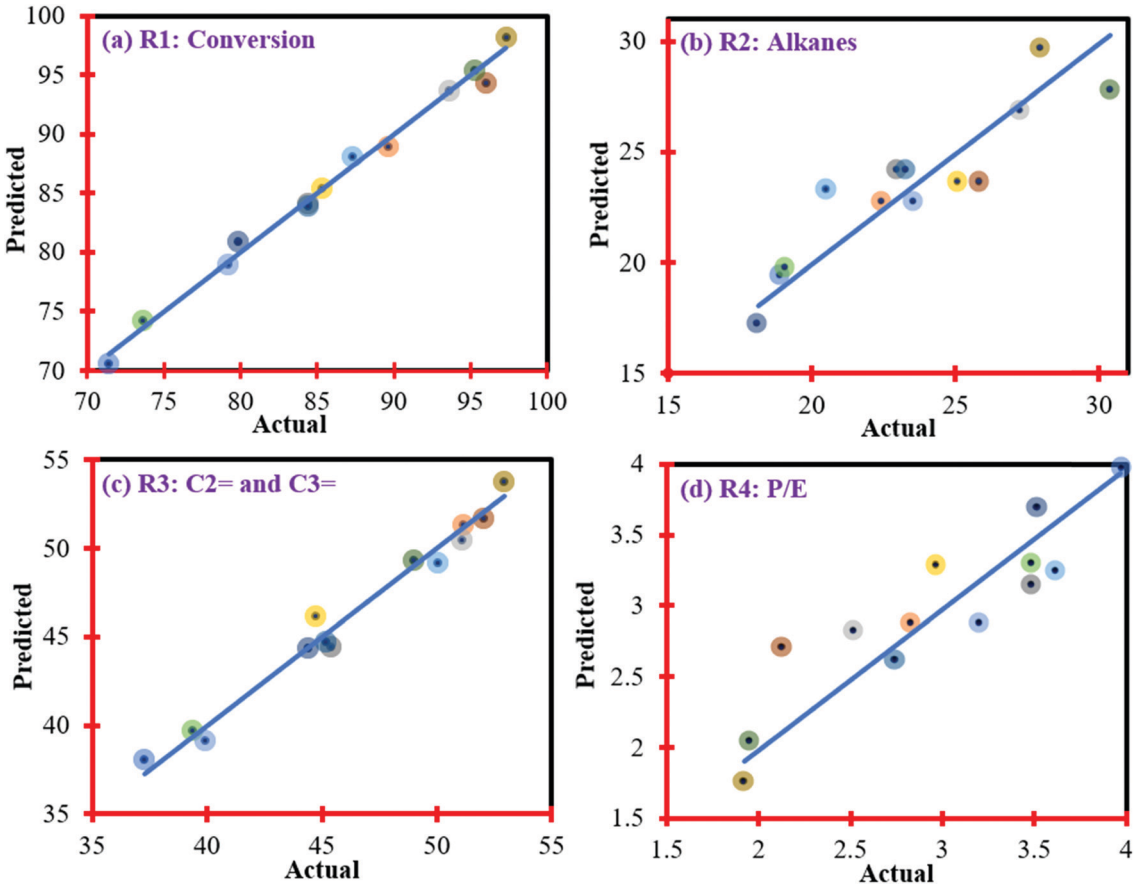

Fig. 7 Comparison of the experimental and predicted values using the equation of the models.

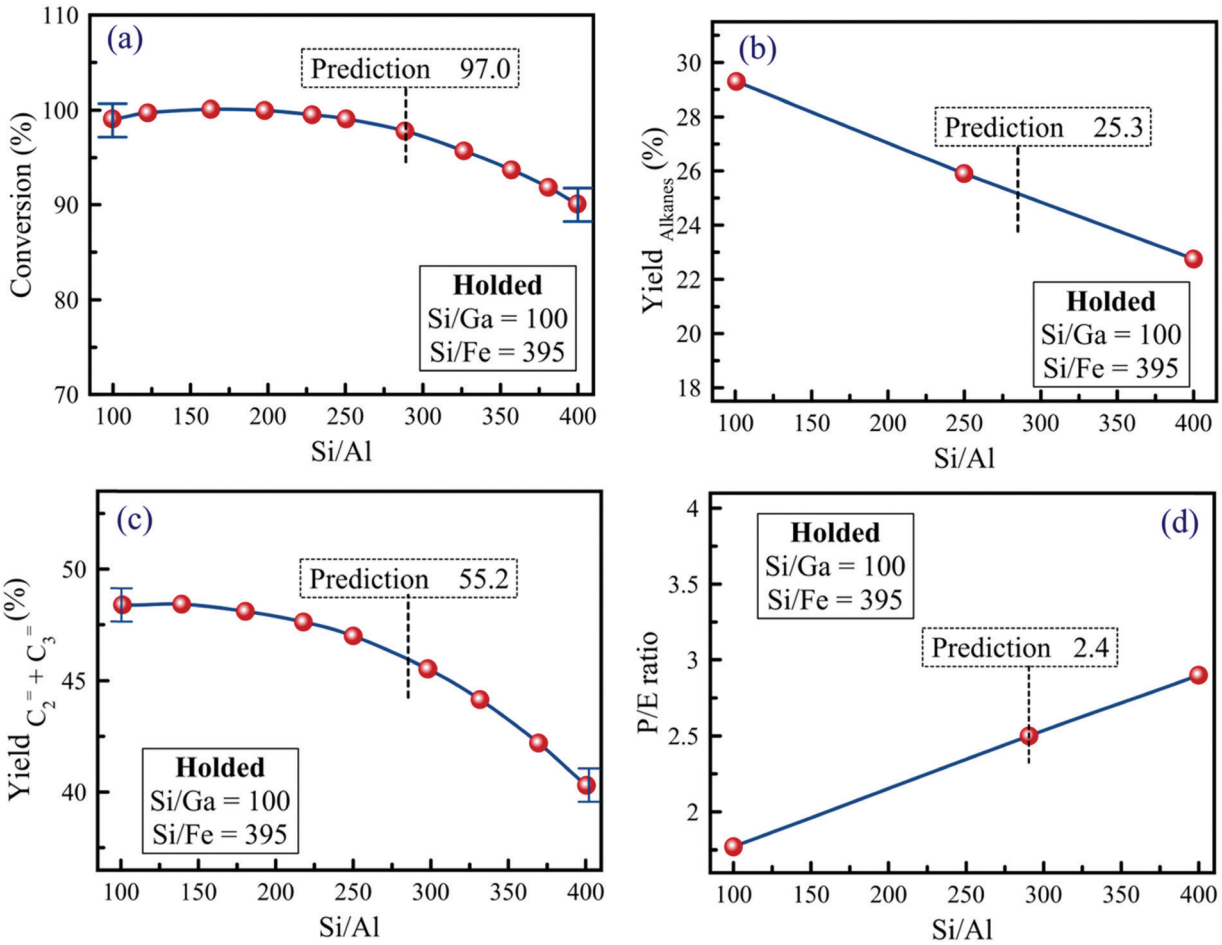

Fig. 8 Effect of the Si/Al main parameter on the responses.

with respect to the appropriate values obtained for the *R*-square, and adjusted and predicted *R*-square parameters (Table 7). Therefore, these models are the basis for interpreting the obtained relations $Y = f(A, B, C)$.

(a) Si/Al effect. According to Table 6, the amount of Al has the strongest impact on all responses because the relevant corresponding *F*-value is higher than all other factors. In fact, SAS, which are mainly composed of skeleton Si–O–Al, are the most important factors in the study of a catalytic process.[26,63] According to Fig. 8, the conversion of hexane was diminished due to the increase of the Si/Al ratio from the approximate range of 200, which can be mainly related to the substantial reduction in the number and strength of SBAS by decreasing Al in the structure.[32,64] The yield of light alkanes was also reduced by increasing the Si/Al ratio due to the reduction in the strength and amount of acid sites, especially SBAS, which are the main centers of hydrogenation/protonation reactions and cracking of heavy alkanes to lighter alkanes.[65,66] According to Fig. 8, the production efficiency of propylene and ethylene decreased with reducing the amount of Al. On the other hand, the P/E ratio increased. According to recent studies, the selectivity of ethylene and that of propylene act in the opposite direction, mainly due to the difference in the weak/strong acid sites. Increasing the W/S ratio increased the selectivity of ethylene, but decreased the selectivity of propylene, while decreasing the W/S ratio led to increased selectivity of propylene and decreased selectivity of ethylene. On the other hand, the decrease of Al in ZSM-5 decreases the W/S ratio, which is probably due to the reduction of non-framework Al.[67] Extra-structural Al increases the W/S ratio by increasing the formation of weak LAS. Therefore, in the synthesized zeolites, with decreasing the Al amount, the W/S ratio decreased, leading to the increase of the P/E ratio. As shown in Fig. 8, the reduction of the Al amount reduced the yield of light olefins by reducing the total number of acid sites, especially the weak Brønsted and Lewis acid sites, which are the most considerable active centers in the formation of light olefins by partial dehydrogenation reactions.[10]

(b) Si/Fe effect. Table 6 shows that the amount of Fe affects all responses. However, it is less effective in all responses compared with Al and even less effective in the production efficiency of light olefins compared with Ga, mainly due to the lower dissociation ability of protons in Si–OH–Fe.

As shown in Fig. 9, decreasing the amount of Fe in the synthesized zeolites led to the linear enhancement of the catalytic activity. In fact, this result showed that increasing the amount of Fe reduced the number and/or strength of SBAS

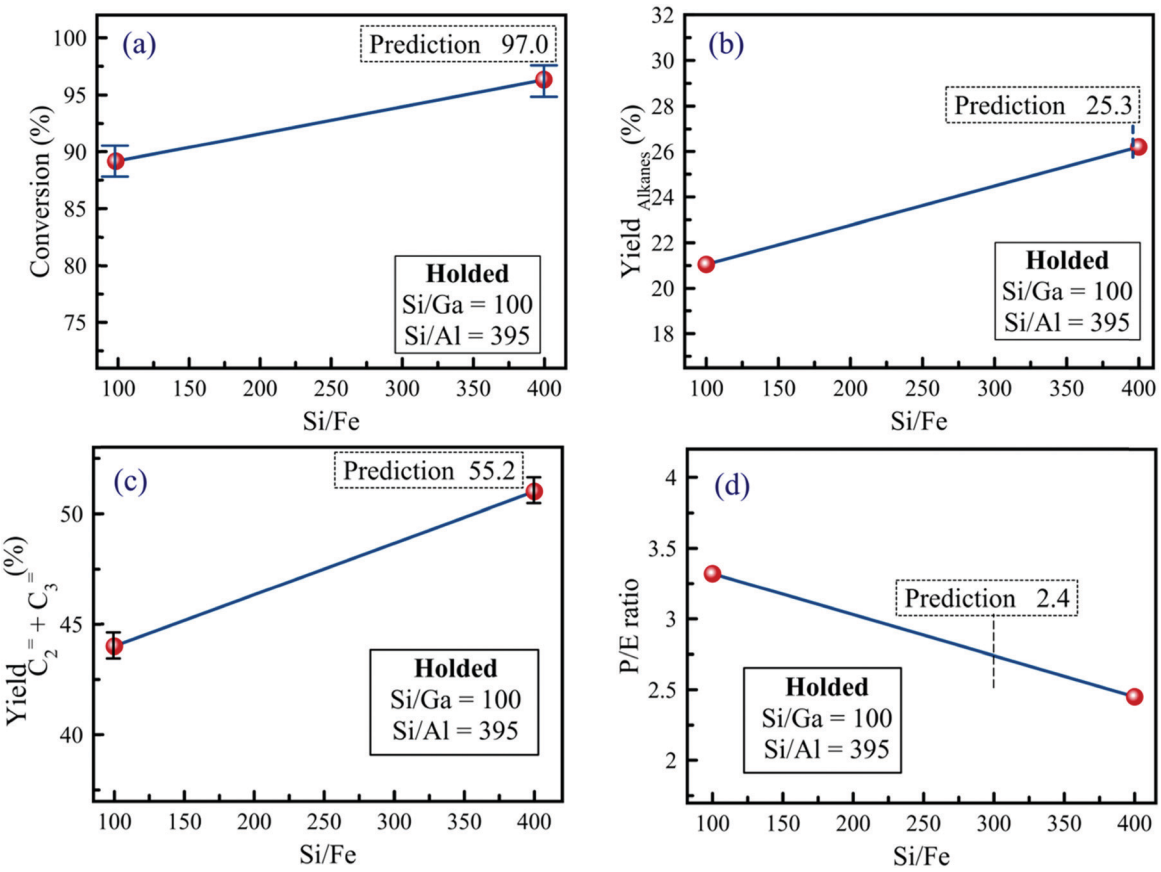

Fig. 9 Effect of the Si/Fe main parameter on the responses.

as the main sites of alkane cracking.[54] Recent studies showed that increasing Fe reduced the WAS and SAS and increased the moderate acid sites in ZSM-5, which ultimately increased the total acid sites. Therefore, the main increase in the number of acid sites is related to the moderate and WAS, which have a limited effect on the process of cracking of alkanes. The principal presence of Fe in the structure of the zeolites was confirmed by H_2-TPR analysis. Therefore, the only reason for decreasing the catalyst activity by increasing Fe was the decreased strength of SBAS, which was related to the increase of the H^+ bond strength in Si–OH–Fe.[53,68] In fact, it seems that with increasing Fe the proton bond in the tetrahedral structure of MFI becomes stronger and its separation requires more energy for hexane cracking by hydrogenation processes, ultimately leading to the reduction of hexane cracking.[69] Moreover, the reduction of Fe increased the yield of alkanes probably due to the increased hydrogenation reactions caused by SBAS. Indeed, the reduction of Fe by increasing the strength of acid sites due to structural proton cleavage increased the hydrogen transfer reactions and consequently the cracking of hexane to lighter alkanes. According to Fig. 9, the reduction of Fe increased the production efficiency of light olefins. In addition, according to the results of hexane conversion and the yield of alkanes, it seems that, with the reduction of Fe, the strength of SBAS increased, which showed its effect in increasing the selectivity of ethylene. As shown in Fig. 9, the P/E ratio decreased with increasing the Si/Fe ratio, which means the increase of ethylene production and decrease of propylene production with the reduction of Fe. Reduction of Fe with increasing the partial dehydrogenation and methylation increased the yield of propylene and ethylene. However, lighter products such as ethylene were produced more due to the higher strength of SBAS.

(c) Si/Ga effect. According to Table 6, the amount of Ga had the lowest effect on the responses and probably had no effect on the yield of alkanes and the P/E ratio, mainly due to the unique intrinsic properties of Ga, such as the low cation electronegativity.[70]

The amount of Ga in the catalytic cracking of hexane demonstrated a much more complex effect than other metals. According to Fig. 10, increasing the Si/Ga ratio to the approximate range of 300 reduced the catalyst activity. However, upon a further decrease of Ga, the hexane conversion increased. In synthetic zeolites, Ga is placed in three forms of tetrahedral substituted in the structure, and gallium oxides and extra-framework Ga species in the cavities, the last being the main acid site for dehydrocyclization reactions in the olefin and aromatic production processes.[71–73] Investigations revealed that decreasing the amount of Ga in synthesized ZSM-5 increased the amount of gallium oxides and extra-framework Ga species.[74] Therefore, the decrease of Ga to the ratio of Si/Ga = 300 increases the formation of extra-framework species. However, by creating extra-framework species,

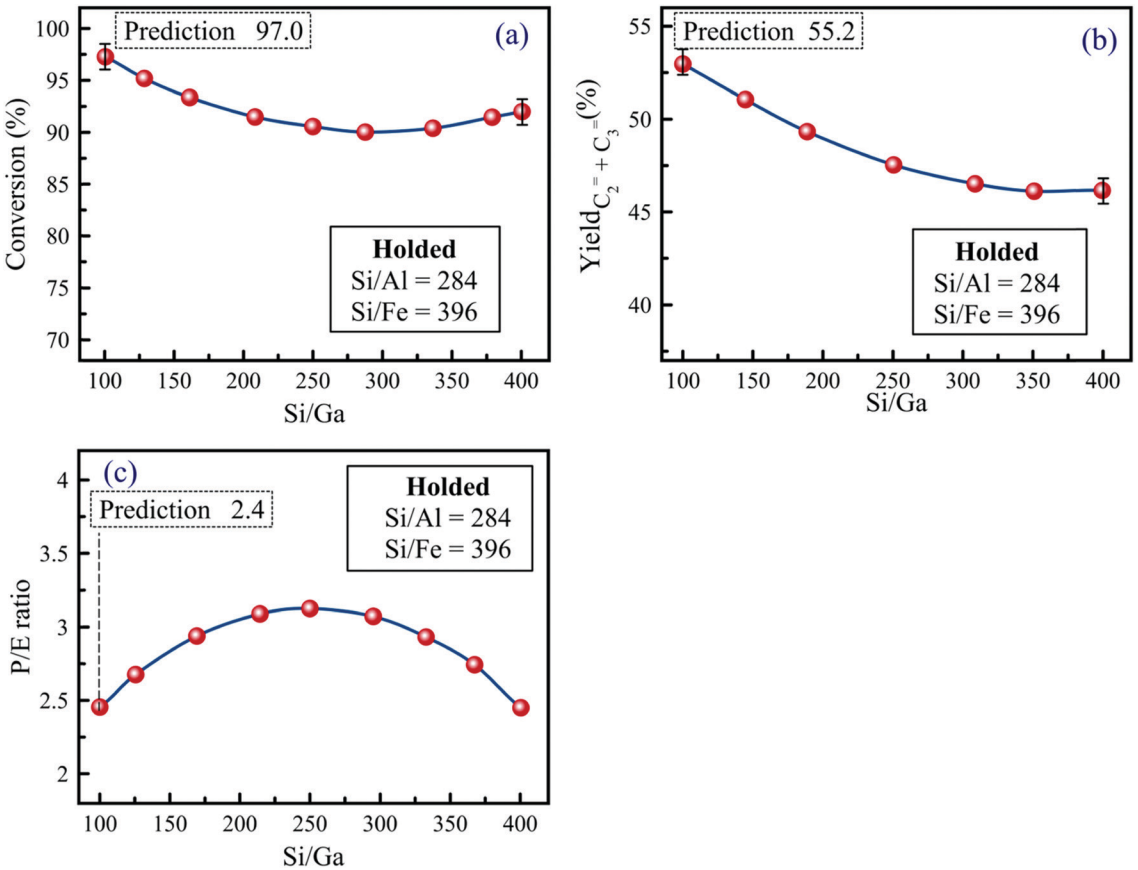

Fig. 10 Effect of the Si/Ga main parameter on the responses.

hexane cracking may be improved at the surface centers before entering the cavities, which ultimately enhances the catalyst activity. According to Fig. 10, with increasing the Si/Ga ratio to approximately 260, the P/E ratio is increased, but then decreased, which means a decrease in propylene and an increase in ethylene production. The Al cation is more electronegative than Ga. Thus the resulting acid strength of the Ga cation is much weaker.[74,75] Therefore, with increasing Ga, it seems that the WAS increase the propylene production by methylation reactions. However, from a certain proportion onwards, where extra-framework sites are increased, far more propylene is formed by methylation of ethylene in the cavities. However, the production efficiency of light olefins decreases linearly with decreasing Ga, indicating the formation of weak and moderate acid sites with increasing Si/Ga ratio. In fact, minor changes from a certain ratio onwards could not affect the overall yield of light olefins, but only enhance partial methylation and dehydrogenation by creating WAS outside the structure.

3.3.2. Interactions. According to Table 6, the amounts of Fe and Ga interact only in the catalytic activity. Fig. 11 shows the effect of variations in Fe in the upper and lower limits of the Si/Ga ratio on the conversion. According to Fig. 11, the decrease in the amount of Fe in both limits increased the activity. Moreover, the conversion of hexane increased with increasing the Si/Fe ratio in the upper and lower limits. In fact, as the amount of Fe decreased, the strength of SBAS increased, ultimately increasing the catalyst activity even though the amount of Ga was reduced in the upper limit, which confirms the effect of Fe.

According to the interactions of Al and Ga in the catalytic activity (Fig. 11), the reduction of Al decreased the catalytic activity in both the upper and lower limits of the Si/Ga ratio, and increased the difference of hexane conversion between the upper and lower limits. At Si/Al ratios below 180, due to the high catalytic activity at a low Si/Ga ratio, less Ga increased the conversion, but more Ga showed more activity. In addition, increasing the Si/Al ratio at both the upper and lower limits of the Si/Ga ratio reduced the total yield of light olefins and increased the distance between the yields of light olefins at the upper and lower limits of the Si/Ga ratio. At the lower limit of the Si/Ga ratio up the Si/Al = 300, decreasing the amount of Ga increased the yield of light olefins until Si/Al = 300, and then decreased the yield of light olefins with a slower slope in comparison with the upper limit. This phenomenon confirms the results obtained from the effect of Ga on the yield of light olefins, because the increase of Ga, a cation with weaker electronegativity, creates more WAS, which are the main centers for the formation of light olefins.

3.3.3. Optimization of the Si/metal ratios. Due to the importance of the responses, the data were optimized using Design Expert software. The optimization was performed in four modes: (1) optimization with the aim of maximum

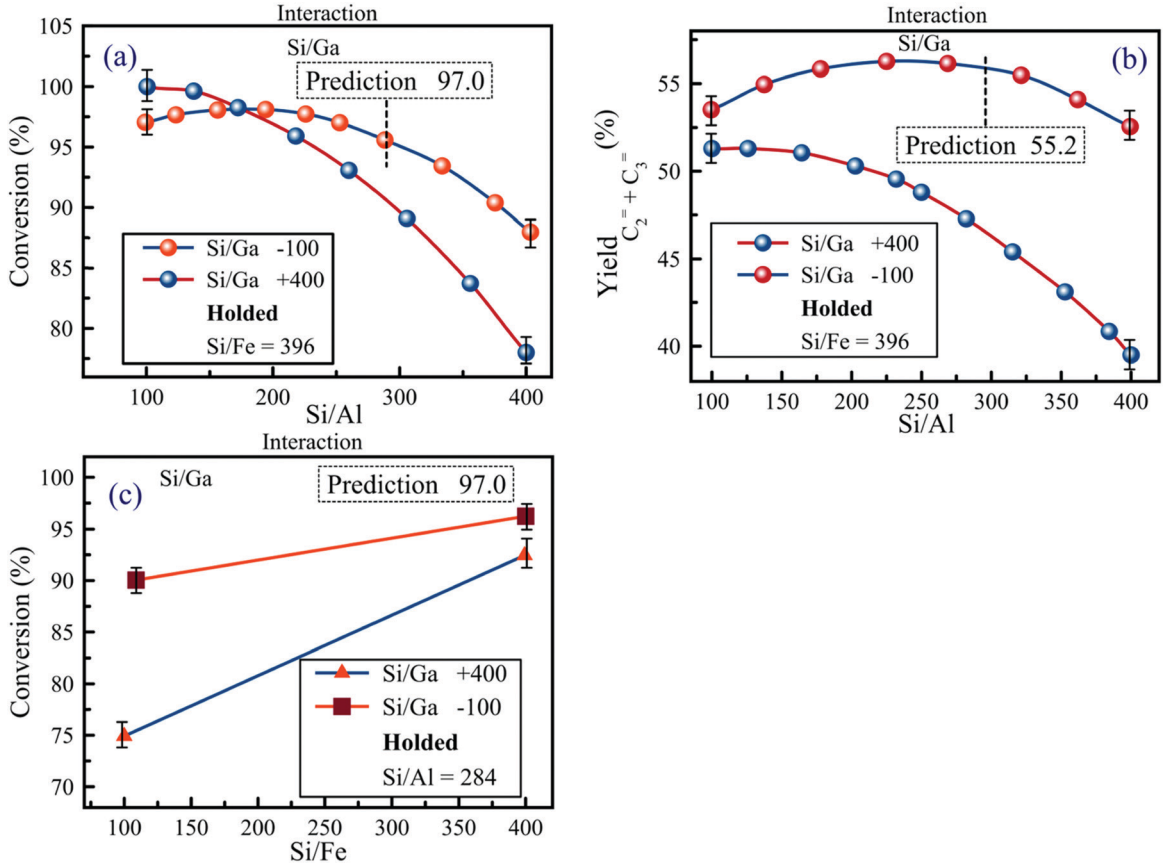

Fig. 11 Valid interactions.

Table 8 Optimization conditions

Response	Quantity	Si/Al	Si/Fe	Si/Ga	Conversion	$Y_{Alkanes}$	$Y_{Olefins}$	P/E
Conversion	Maximum	110	377	123	96.8	29.0	52.8	2.0
$Y_{Alkanes}$	Minimum	370	130	130	81.1	18.5	44.6	3.7
$Y_{Olefins}$	Maximum	110	377	123	96.8	29.0	52.8	2.0
P/E	Maximum	317	123	263	75.5	19.6	41.2	4.0

conversion, (2) optimization with the aim of the minimum yield of alkanes, (3) optimization with the aim of the maximum yield of light olefins and (4) optimization with the aim of the maximum P/E ratio. As observed in Table 8, the optimal conditions in the two cases of maximum conversion and maximum yield of light olefins were equal. On the other hand, the significance of the responses corresponding to the maximum conversion and maximum yield of light olefins is higher than that of the other two responses. Therefore, considering the significance of light olefins and the subsequent catalytic activity, the optimal catalyst conditions can be defined as follows: Si/Al = 110; Si/Fe = 377; Si/Ga = 123.

4. Conclusions

In this work, the synergistic effect of incorporating Fe and Ga into the ZSM-5 structure in the production of light olefins from *n*-hexane was completely investigated. Nano zeolites were synthesized in fluorine medium using colloidal silica and TPAOH to maximize the incorporation of metals in the structure. Experimental design by the D-optimal method was utilized to investigate the effect of three factors on four responses. The predicted values of the D-optimal experimental design showed acceptable agreement with the experimental results along with appropriate R^2, R^2 adjusted and R^2 predicted. The study of the structural properties showed the synergistic effect of Fe and Ga on the reduction of the particle size by increasing the nucleation rate, which was probably due to the variation in atomic radii. In addition, the absence of extra-framework species of Ga and Fe was confirmed by studying the acidic properties, and Fe, Al and Ga increased the number of total acid sites, the strength of SAS and the strength of WAS, respectively. The simultaneous presence of Fe and Ga also improved the number of WAS. The optimal conditions for obtaining the maximum conversion, light olefins, and P/E ratio and minimum alkanes as the responses were Si/Al = 110; Si/Fe = 377; Si/Ga = 123.

Conflicts of interest

There are no conflicts to declare.

References

1 V. Blay, B. Louis, R. Miravalles, T. Yokoi, K. A. Peccatiello, M. Clough and B. Yilmaz, *ACS Catal.*, 2017, **7**, 6542–6566.
2 X. Dong, S. Shaikh, J. R. Vittenet, J. Wang, Z. Liu, K. D. Bhatte, O. Ali, W. Xu, I. Osorio and Y. Saih, *ACS Sustainable Chem. Eng.*, 2018, **6**, 15832–15840.
3 K. Wang, J. Zhang, S. Fan, X. Peng, N. Tsubaki and T. Zhao, *New J. Chem.*, 2021, **45**, 4860–4866.
4 P. Cnudde, K. De Wispelaere, L. Vanduyfhuys, R. Demuynck, J. Van der Mynsbrugge, M. Waroquier and V. Van Speybroeck, *ACS Catal.*, 2018, **8**, 9579–9595.
5 X. Hou, Y. Qiu, E. Yuan, F. Li, Z. Li, S. Ji, Z. Yang, G. Liu and X. Zhang, *Appl. Catal., A*, 2017, **543**, 51–60.
6 M. Arsalanfar, *New J. Chem.*, 2020, **44**, 18457–18468.
7 U. Olsbye, S. Svelle, M. Bjørgen, P. Beato, T. V. Janssens, F. Joensen, S. Bordiga and K. P. Lillerud, *Angew. Chem., Int. Ed.*, 2012, **51**, 5810–5831.
8 M. Rostami Sakha, S. Soltanali, D. Salari, M. Rashidzadeh and P. Halimi Tabrizi, *J. Solid State Chem.*, 2021, **301**, 122342.
9 B. K. Yalcin and B. Ipek, *Appl. Catal., A*, 2021, **610**, 117915.
10 T. Ma, L. Zhang, Y. Song, Y. Shang, Y. Zhai and Y. Gong, *Catal. Sci. Technol.*, 2018, **8**, 1923–1935.
11 S. Mitchell, M. Boltz, J. Liu and J. Pérez-Ramírez, *Catal. Sci. Technol.*, 2017, **7**, 64–74.
12 X. Hou, Y. Qiu, X. Zhang and G. Liu, *Chem. Eng. J.*, 2017, **307**, 372–381.
13 S. Xin, Q. Wang, J. Xu, Y. Chu, P. Wang, N. Feng, G. Qi, J. Trébosc, O. Lafon and W. Fan, *Chem. Sci.*, 2019, **10**, 10159–10169.
14 B. C. Knott, C. T. Nimlos, D. J. Robichaud, M. R. Nimlos, S. Kim and R. Gounder, *ACS Catal.*, 2018, **8**, 770–784.
15 C. Wang, L. Zhang, X. Huang, Y. Zhu, G. K. Li, Q. Gu, J. Chen, L. Ma, X. Li and Q. He, *Nat. Commun.*, 2019, **10**, 1–8.
16 I. Yarulina, A. D. Chowdhury, F. Meirer, B. M. Weckhuysen and J. Gascon, *Nat. Catal.*, 2018, **1**, 398–411.
17 T. Yokoi, H. Mochizuki, S. Namba, J. N. Kondo and T. Tatsumi, *J. Phys. Chem. C*, 2015, **119**, 15303–15315.
18 J. Dědeček, E. Tabor and S. Sklenak, *ChemSusChem*, 2019, **12**, 556–576.
19 S. Svelle, F. Joensen, J. Nerlov, U. Olsbye, K.-P. Lillerud, S. Kolboe and M. Bjørgen, *J. Am. Chem. Soc.*, 2006, **128**, 14770–14771.
20 E. Dib, T. Mineva, P. Gaveau, E. Véron, V. Sarou-Kanian, F. Fayon and B. Alonso, *J. Phys. Chem. C*, 2017, **121**, 15831–15841.
21 K. Chen, M. Abdolrahmani, S. Horstmeier, T. N. Pham, V. T. Nguyen, M. Zeets, B. Wang, S. Crossley and J. L. White, *ACS Catal.*, 2019, **9**, 6124–6136.
22 A. Ghorbanpour, J. D. Rimer and L. C. Grabow, *Catal. Commun.*, 2014, **52**, 98–102.
23 J. Dědeček, Z. Sobalík and B. Wichterlová, *Catal. Rev.: Sci. Eng.*, 2012, **54**, 135–223.
24 E. Tabor, M. Bernauer, B. Wichterlová and J. Dedecek, *Catal. Sci. Technol.*, 2019, **9**, 4262–4275.
25 S. Wang, P. Wang, Z. Qin, Y. Chen, M. Dong, J. Li, K. Zhang, P. Liu, J. Wang and W. Fan, *ACS Catal.*, 2018, **8**, 5485–5505.
26 Z. Wang, L. A. O'Dell, X. Zeng, C. Liu, S. Zhao, W. Zhang, M. Gaborieau, Y. Jiang and J. Huang, *Angew. Chem., Int. Ed.*, 2019, **58**, 18061–18068.
27 S. Bailleul, I. Yarulina, A. E. Hoffman, A. Dokania, E. Abou-Hamad, A. D. Chowdhury, G. Pieters, J. Hajek, K. De Wispelaere and M. Waroquier, *J. Am. Chem. Soc.*, 2019, **141**, 14823–14842.
28 A. Vjunov, J. L. Fulton, T. Huthwelker, S. Pin, D. Mei, G. K. Schenter, N. Govind, D. M. Camaioni, J. Z. Hu and J. A. Lercher, *J. Am. Chem. Soc.*, 2014, **136**, 8296–8306.
29 C. Li, A. Vidal-Moya, P. J. Miguel, J. Dedecek, M. Boronat and A. Corma, *ACS Catal.*, 2018, **8**, 7688–7697.
30 T. Liang, J. Chen, Z. Qin, J. Li, P. Wang, S. Wang, G. Wang, M. Dong, W. Fan and J. Wang, *ACS Catal.*, 2016, **6**, 7311–7325.
31 J. Li, H. Ma, Y. Chen, Z. Xu, C. Li and W. Ying, *Chem. Commun.*, 2018, **54**, 6032–6035.
32 A. Janda and A. T. Bell, *J. Am. Chem. Soc.*, 2013, **135**, 19193–19207.
33 S. Müller, Y. Liu, F. M. Kirchberger, M. Tonigold, M. Sanchez-Sanchez and J. A. Lercher, *J. Am. Chem. Soc.*, 2016, **138**, 15994–16003.
34 J. Li, M. Liu, X. Guo, S. Zeng, S. Xu, Y. Wei, Z. Liu and C. Song, *Ind. Eng. Chem. Res.*, 2018, **57**, 15375–15384.
35 Y. Ji, H. Yang and W. Yan, *Mol. Catal.*, 2018, **448**, 91–99.
36 Q. Shang, G. Xu, N. Tang, C. Wu, S. Chen and Y. Cong, *Microporous Mesoporous Mater.*, 2019, **288**, 109616.
37 P. Losch, A. B. Pinar, M. G. Willinger, K. Soukup, S. Chavan, B. Vincent, P. Pale and B. Louis, *J. Catal.*, 2017, **345**, 11–23.
38 Y. Ji, H. Yang and W. Yan, *Catalysts*, 2017, **7**, 367.
39 Y. Nakasaka, J.-i. Nishimura, T. Tago and T. Masuda, *Chem. Eng. J.*, 2015, **278**, 159–165.
40 S. Kim, G. Park, M. H. Woo, G. Kwak and S. K. Kim, *ACS Catal.*, 2019, **9**, 2880–2892.
41 H. Konno, R. Ohnaka, J.-I. Nishimura, T. Tago, Y. Nakasaka and T. Masuda, *Catal. Sci. Technol.*, 2014, **4**, 4265–4273.
42 G. Song, W. Chen, P. Dang, Y. Wang and F. Li, *R. Soc. Open Sci.*, 2018, **5**, 181691.
43 Y. Zhang, X. Han and S. Che, *Chem. Commun.*, 2019, **55**, 810–813.
44 S. Zhao, W. D. Wang, L. Wang, W. Schwieger, W. Wang and J. Huang, *ACS Catal.*, 2020, **10**, 1185–1194.
45 H. Li, Y. Wang, C. Fan, C. Sun, X. Wang, C. Wang, X. Zhang and S. Wang, *Appl. Catal., A*, 2018, **551**, 34–48.
46 N. Rahimi and R. Karimzadeh, *Appl. Catal., A*, 2011, **398**, 1–17.
47 X. Su, Y. Fang, X. Bai and W. Wu, *Ind. Eng. Chem. Res.*, 2019, **58**, 20543–20552.
48 K. Iisa, Y. Kim, K. A. Orton, D. J. Robichaud, R. Katahira, M. J. Watson, E. C. Wegener, M. R. Nimlos, J. A. Schaidle, C. Mukarakate and S. Kim, *Green Chem., Green Chem.*, 2020, **22**, 2403–2418.
49 X. Li, A.-A. Alwakwak, F. Rezaei, A. A. Rownaghi and A. C. S. Appl, *Energy Mater.*, 2018, **1**, 2740–2748.

50 W. Dai, L. Yang, C. Wang, X. Wang, G. Wu, N. Guan, U. Obenaus, M. Hunger and L. Li, *ACS Catal.*, 2018, **8**, 1352–1362.
51 K. Van der Borght, V. V. Galvita and G. B. Marin, *Appl. Catal., A*, 2015, **492**, 117–126.
52 M. Hu, C. Wang, X. Gao, Y. Chu, G. Qi, Q. Wang, G. Xu, J. Xu and F. Deng, *ACS Catal.*, 2020, **10**, 4299–4305.
53 X. Jiang, X. Su, X. Bai, Y. Li, L. Yang, K. Zhang, Y. Zhang, Y. Liu and W. Wu, *Microporous Mesoporous Mater.*, 2018, **263**, 243–250.
54 K. Bian, A. Zhang, H. Yang, B. Fan, S. Xu, X. Guo and C. Song, *Ind. Eng. Chem. Res.*, 2020, **59**, 22413–22421.
55 Z.-Y. Du, B.-B. Zhang, T.-S. Chen, Y. Betancur and W.-Y. Li, *Energy Fuels*, 2019, **33**, 10176–10184.
56 Y. T. Cheng, J. Jae, J. Shi, W. Fan and G. W. Huber, *Angew. Chem., Int. Ed.*, 2012, **124**, 1416–1419.
57 Z. Li, A. W. Lepore, M. F. Salazar, G. S. Foo, B. H. Davison, Z. Wu and C. K. Narula, *Green Chem.*, 2017, **19**, 4344–4352.
58 Z. Hajjar, M. Kazemeini, A. Rashidi and S. Soltanali, *J. Taiwan Inst. Chem. Eng.*, 2017, **78**, 566–575.
59 J. Sjöblom, K. Papadakis, D. Creaser and C. I. Odenbrand, *Catal. Today*, 2005, **100**, 243–248.
60 G. B. Ferraris, P. Forzatti, G. Emig and H. Hofmann, *Chem. Eng. Sci.*, 1984, **39**, 81–85.
61 R. Feng, X. Yan, X. Hu, Y. Zhang, J. Wu and Z. Yan, *Appl. Catal., A*, 2020, **594**, 117464.
62 M. Thommes, K. Kaneko, A. V. Neimark, J. P. Olivier, F. Rodriguez-Reinoso, J. Rouquerol and K. S. Sing, *Pure Appl. Chem.*, 2015, **87**, 1051–1069.
63 T. Biligetu, Y. Wang, T. Nishitoba, R. Otomo, S. Park, H. Mochizuki, J. N. Kondo, T. Tatsumi and T. Yokoi, *J. Catal.*, 2017, **353**, 1–10.
64 Y.-H. Yeh, R. J. Gorte, S. Rangarajan and M. Mavrikakis, *J. Phys. Chem. C*, 2016, **120**, 12132–12138.
65 S. Park, T. Biligetu, Y. Wang, T. Nishitoba, J. N. Kondo and T. Yokoi, *Catal. Today*, 2018, **303**, 64–70.
66 M. Bernauer, E. Tabor, V. Pashkova, D. Kaucký, Z. Sobalík, B. Wichterlová and J. Dedecek, *J. Catal.*, 2016, **344**, 157–172.
67 I. Yarulina, K. De Wispelaere, S. Bailleul, J. Goetze, M. Radersma, E. Abou-Hamad, I. Vollmer, M. Goesten, B. Mezari and E. J. Hensen, *Nat. Chem.*, 2018, **10**, 804–812.
68 D. S. Lima and O. W. Perez-Lopez, *Renewable Energy*, 2019, **136**, 828–836.
69 M. Rostamizadeh and F. Yaripour, *Fuel*, 2016, **181**, 537–546.
70 M. Xin, E. Xing, X. Gao, Y. Wang, Y. Ouyang, G. Xu, Y. Luo and X. Shu, *Ind. Eng. Chem. Res.*, 2019, **58**, 6970–6981.
71 P. Gao, Q. Wang, J. Xu, G. Qi, C. Wang, X. Zhou, X. Zhao, N. Feng, X. Liu and F. Deng, *ACS Catal.*, 2018, **8**, 69–74.
72 Y.-H. Yeh and R. J. Gorte, *Ind. Eng. Chem. Res.*, 2016, **55**, 12795–12805.
73 X. Su, Y. Fang, P. Gao, Y. Liu, G. Hou, X. Bai and W. Wu, *Microporous Mesoporous Mater.*, 2020, **306**, 110388.
74 Z. Han, F. Zhou, Y. Liu, K. Qiao, H. Ma, L. Yu and G. Wu, *J. Taiwan Inst. Chem. Eng.*, 2019, **103**, 149–159.
75 G. Krishnamurthy, A. Bhan and W. N. Delgass, *J. Catal.*, 2010, **271**, 370–385.

